where

$$\mathbf{K}_{\alpha\alpha} = \int_{\Omega} \left(\frac{1}{|V|} \int_{Y_0} [{}_0\chi^e]^T [B^e]^T [A][B^e][{}_0\chi^e] dY \right) dX, \tag{51}$$

$$\mathbf{K}_{\alpha u} = -\int_{\Omega} \left(\frac{1}{|V|} \int_{Y_0} [{}_0\chi^e]^T [B^e]^T [A] dY \right) [\overline{B^e}] dX, \tag{52}$$

$$\mathbf{K}_{u\alpha} = -\int_{\Omega} [\overline{B^e}]^T \left(\frac{1}{|V|} \int_{Y_0} [A][B^e][{}_0\chi^e] dY \right) dX, \tag{53}$$

$$\mathbf{K}_{uu} = \int_{\Omega} [\overline{B^e}]^T \left(\frac{1}{|V|} \int_{Y_0} [A] dY \right) [\overline{B^e}] dX, \tag{54}$$

$$\{\mathbf{r}_u\} = F_{ext} - \int_{\Omega} [\overline{B^e}]^T \left(\frac{1}{|V|} \int_{Y_0} [\Pi] dY \right) dX, \tag{55}$$

$$\{\mathbf{r}_\alpha\} = \int_{\Omega} \left(\frac{1}{|V|} \int_{Y_0} [{}_0\chi^e]^T [B^e]^T [\Pi] dY \right) dX. \tag{56}$$

We obtain the matrix with unknowns $\Delta\alpha$ and $\Delta\mathbf{u}$. Because the NDOF of the matrix is reduced to (NDOF of macrostructure + quadrature point of macrostructure $\times$ 9), significant computational cost is saved.

This technique is, however, an approximate means of achieving equilibrium in a range of displacements representing linear combinations of χ_0, as it is clear from Eq. (56) that χ_0 has an effect on the equilibrium. In this way, to approximate the deformation in limited deformation patterns, an approximation error is created depending on the analysis case [15].

3 Algorithm for nonlinear homogenization method

3.1 Generalized algorithm

In Eq. (22), $\{\Delta w\}$ can be statically condensed at the element quadrature point level and becomes

$$\{\Delta\mathbf{w}\} = \mathbf{K}_{ww}^{-1}(\{\mathbf{r}_w\} - \mathbf{K}_{wu}\{\Delta\mathbf{u}\}). \tag{57}$$

$\{\Delta w\}$ vanishes when the above equation is substituted in the macroscopic equilibrium equation

$$(\mathbf{K}_{uu} - \mathbf{K}_{uw}\mathbf{K}_{ww}^{-1}\mathbf{K}_{wu})\{\Delta\mathbf{u}\} = \{\mathbf{r}_u\} - \mathbf{K}_{uw}\mathbf{K}_{ww}^{-1}\{\mathbf{r}_w\}. \tag{58}$$

Now, the microscopic equilibrium hypothesized for $\overline{\mathbf{F}}$ at this time is

$$\{\mathbf{r}_w\} = 0. \tag{59}$$

By using Eqs. (43) and (57), we obtain [5]

$$\{\Delta\mathbf{w}\} = -\mathbf{K}_{ww}^{-1}\mathbf{K}_{wu}\{\Delta\mathbf{u}\} = -[\chi][\overline{\mathbf{B}}]\{\Delta\mathbf{u}\}. \tag{60}$$

By using Eqs. (43), (57), and (58) we can represent

$$(\mathbf{K}_{uu} - \mathbf{K}_{uw}[\chi][\overline{\mathbf{B}}])\{\Delta\mathbf{u}\} = \{\mathbf{r}_u\}, \tag{61}$$

where $(\mathbf{K}_{uu} - \mathbf{K}_{uw}[\chi][\overline{\mathbf{B}}])$ is called the homogenized tangent stiffness.

In differential equation form, from Eqs. (14), (17), and (31), this becomes

$$\int_{\Omega} \delta\overline{\mathbf{F}} : \left(\frac{1}{|V|} \int_{Y_0} \left(\mathbf{A} : (\mathbf{I} - \nabla_Y \chi) \right) dY \right) : \Delta\overline{\mathbf{F}} dX = \overline{\mathbf{F}}_{ext} - \int_{\Omega} \delta\overline{\mathbf{F}} : \left(\frac{1}{|V|} \int_{Y_0} \Pi dY \right) dX. \tag{62}$$

Microscopic equilibrium, Eq. (59),

$$r_w = \int_{Y_0} \delta\tilde{\mathbf{Z}} : \Pi dY = \mathbf{0}, \tag{63}$$

is a prerequisite of the above equation. To satisfy this nonlinear prerequisite, a Newton–Raphson iteration is needed. Thus the above equation is linearized with respect to $\mathbf{w}$ while $\overline{\mathbf{F}}$ is fixed, and then discretized by the finite element method using Eq. (19). At each quadrature point, the linearized self-equilibrated equation becomes

$$\int_{Y_0} [B^e]^T [A][B^e] dY \{\Delta\mathbf{w}^{\mathcal{Q}}\} = -\int_{Y_0} [B^e]^T [\Pi] dY. \tag{64}$$

In the generalized algorithm, it is necessary to compute three different calculations in each iteration.

1. Update macroscopic tangential homogenization χ using Eq. (36).
2. Solve microscopic equilibrium problem, Eq. (63), and obtain the convergence solution $\{\mathbf{w}\}$ while $\overline{\mathbf{F}}$ is fixed.
3. Solve the linearized macroscopic equilibrium equation, Eq. (61), to obtain $\{\mathbf{u}\}$.

Processes 1 and 2 need to be solved at all quadrature points of the macrostructure and it is known that this contributes the most to the calculation load [6]. These processes require prohibitive computational cost and actual numerical simulation is difficult.

3.2 Block LU factorization algorithm

We now present an algorithm that decreases the residual of each scale simultaneously using the block LU factorization

algorithm without microscopic convergence in the macroscopic iteration as in the conventional algorithm. By block LU factorization, Eq. (22) becomes

$$\begin{bmatrix} \mathbf{K}_{ww} & \mathbf{0} \\ \mathbf{K}_{uw} & \mathbf{S} \end{bmatrix} \begin{bmatrix} \mathbf{I} & \mathbf{K}_{ww}^{-1}\mathbf{K}_{wu} \\ \mathbf{0} & \mathbf{I} \end{bmatrix} \begin{Bmatrix} \Delta\mathbf{w} \\ \Delta\mathbf{u} \end{Bmatrix} = \begin{Bmatrix} \mathbf{r}_w \\ \mathbf{r}_u \end{Bmatrix}, \tag{65}$$

where $\mathbf{S}$ is called the Schur-Complement. Referring to Eq. (43),

$$\begin{aligned} \mathbf{S} &= \mathbf{K}_{uu} - \mathbf{K}_{uw}\mathbf{K}_{ww}^{-1}\mathbf{K}_{wu} \\ &= \mathbf{K}_{uu} - \mathbf{K}_{uw}[\chi][\overline{\mathbf{B}}] \\ &= \mathbf{K}_{uu} - [\overline{\mathbf{B}}]^T[\chi]^T\mathbf{K}_{ww}[\chi][\overline{\mathbf{B}}], \end{aligned} \tag{66}$$

which corresponds to the homogenized tangent stiffness of Eq. (61). The solution process for Eq. (65) is composed of the forward substitution

$$\begin{bmatrix} \mathbf{K}_{ww} & \mathbf{0} \\ \mathbf{K}_{uw} & \mathbf{S} \end{bmatrix} \begin{Bmatrix} \Delta\tilde{\mathbf{w}} \\ \Delta\tilde{\mathbf{u}} \end{Bmatrix} = \begin{Bmatrix} \mathbf{r}_w \\ \mathbf{r}_u \end{Bmatrix}, \tag{67}$$

and the backward substitution

$$\begin{Bmatrix} \Delta\tilde{\mathbf{w}} \\ \Delta\tilde{\mathbf{u}} \end{Bmatrix} = \begin{bmatrix} \mathbf{I} & \mathbf{K}_{ww}^{-1}\mathbf{K}_{wu} \\ \mathbf{0} & \mathbf{I} \end{bmatrix} \begin{Bmatrix} \Delta\mathbf{w} \\ \Delta\mathbf{u} \end{Bmatrix}. \tag{68}$$

Then, from Eqs. (43), (67), and (68),

$$\mathbf{K}_{ww}\{\Delta\tilde{\mathbf{w}}\} = \{\mathbf{r}_w\}, \tag{69}$$

$$\mathbf{S}\{\Delta\mathbf{u}\} = \{\mathbf{r}_u\} - \mathbf{K}_{uw}\{\Delta\tilde{\mathbf{w}}\}, \tag{70}$$

$$\begin{aligned} \{\Delta\mathbf{w}\} &= \{\Delta\tilde{\mathbf{w}}\} - \mathbf{K}_{ww}^{-1}\mathbf{K}_{wu}\{\Delta\mathbf{u}\} \\ &= \{\Delta\tilde{\mathbf{w}}\} - [\chi]\Delta\overline{\mathbf{F}}, \end{aligned} \tag{71}$$

hold. The calculation process is described below.

1. Solve linearized microscopic equilibrium equation, Eq. (69), to obtain $\{\Delta\mathbf{w}\}$.
2. Solve linearized macroscopic equilibrium equation, Eq. (70), to obtain $\{\Delta\mathbf{u}\}$. Note that this equation is equivalent to Eq. (58).
3. Update $\{\Delta\mathbf{w}\}$ using Eq. (71). We have already obtained $[\chi]$ from the calculation of $\mathbf{S}$.

Three matrices, namely the micro, macro, and Schur-Complement, need to be solved at each iteration. Although the computational cost of this algorithm is expected to be lower than that of the generalized algorithm since equilibrium of the microstructure is not required at every iteration, the Schur-Complement update is still relatively expensive as described above. A similar algorithm for a differential equation using the Block-Newton method has been proposed by Yamada and Matsui [19].

3.3 Approximation of schur-complement in micro–macro coupled equation

In the block LU factorization algorithm described in the previous subsection, the linearized equations for the microstructure are solved first and then the increment for the macro-displacements is solved using the Schur-Complement that reflects the micro–macro interactions. These two steps essentially define the computational cost because the third step can be solved efficiently by reusing the characteristic deformation that has already been computed in the evaluation of the Schur-Complement in the second step. Although the macroscopic equilibrium conditions must be satisfied as well as the microscopic ones by making a convergence judgment for the residuals, the Schur-Complement is a tangent stiffness for prediction and does not influence the equilibrium directly. Hence, one of the requirements for efficient nonlinear homogenization algorithms is to approximate the Schur-Complement effectively. In this regard, we propose the two algorithms given below.

A simple method is to approximate the Schur-Complement using the previously calculated characteristic deformation ${}_0\chi$ as in

$$\begin{aligned} \mathbf{S} &= \mathbf{K}_{uu} - \mathbf{K}_{uw}[\chi][\overline{\mathbf{B}}] \\ &\doteqdot \mathbf{K}_{uu} - \mathbf{K}_{uw}[{}_0\chi][\overline{\mathbf{B}}] \\ &= \mathbf{K}_{uu} - [\overline{\mathbf{B}}]^T[\chi]^T\mathbf{K}_{ww}[{}_0\chi][\overline{\mathbf{B}}], \end{aligned} \tag{72}$$

that is,

$$[\chi]^T\mathbf{K}_{ww}[\chi] \doteqdot [\chi]^T\mathbf{K}_{ww}[{}_0\chi], \tag{73}$$

is employed from Eq. (66). Henceforth, this method is referred to as the modified block LU factorization algorithm (MBFA). The other approach is to make use of the aforementioned Mode Superposition method in the approximation of the Schur-Complement. The calculation process and an interpretation thereof are given below.

1. Solve the linearized microscopic equilibrium equation, Eq. (69), to obtain $\{\Delta\tilde{\mathbf{w}}\}$.
2. From Eq. (50), solve the mode superposition-based linearized micro–macro coupled equation

$$\begin{bmatrix} \mathbf{K}_{\alpha\alpha} & \mathbf{K}_{\alpha u} \\ \mathbf{K}_{u\alpha} & \mathbf{K}_{uu} \end{bmatrix} \begin{Bmatrix} \Delta\alpha \\ \Delta\mathbf{u} \end{Bmatrix} = \begin{Bmatrix} \mathbf{r}_\alpha \\ \mathbf{r}_u \end{Bmatrix}, \tag{74}$$

   to obtain $\{\Delta\mathbf{u}\}$. Then, $\mathbf{S}$ is approximated by the range of the mode superposition method and the update of $\mathbf{S}$ can be omitted.
3. The assumption of the mode superposition method follows from Eqs. (46), (47), and (71), and $\{\Delta\mathbf{w}\}$ is updated using

$$\{\Delta \mathbf{w}\} = \{\Delta \tilde{\mathbf{w}}\} - [_0\chi]\{\Delta\alpha\}. \tag{75}$$

The meaning of the algorithm is now given. Block LU factorization is applied to Eq. (74) yielding

$$\mathbf{K}_{\alpha\alpha}\{\Delta\tilde{\alpha}\} = \{\mathbf{r}_\alpha\}, \tag{76}$$

$$(\mathbf{K}_{uu} - \mathbf{K}_{u\alpha}\mathbf{K}_{\alpha\alpha}^{-1}\mathbf{K}_{\alpha u})\{\Delta\mathbf{u}\} = \{\mathbf{r}_u\} - \mathbf{K}_{u\alpha}\{\Delta\tilde{\alpha}\}, \tag{77}$$

$$\{\Delta\alpha\} = \{\Delta\tilde{\alpha}\} - \mathbf{K}_{\alpha\alpha}^{-1}\mathbf{K}_{\alpha u}\{\Delta\mathbf{u}\}. \tag{78}$$

In Eq. (77), the macroscopic displacement is updated using

$$(\mathbf{K}_{uu} - \mathbf{K}_{u\alpha}\mathbf{K}_{\alpha\alpha}^{-1}\mathbf{K}_{\alpha u}), \tag{79}$$

which can be considered an approximation of the homogenized tangent stiffness. Then, using Eqs. (43) and (66), the Schur-Complement becomes

$$\begin{aligned}
\mathbf{S} &= \mathbf{K}_{uu} - \mathbf{K}_{uw}[\chi][\overline{\mathbf{B}}] \\
&= \mathbf{K}_{uu} - \mathbf{K}_{uw}[\chi]([\chi]^T\mathbf{K}_{ww}[\chi])^{-1}([\chi]^T\mathbf{K}_{ww}[\chi])[\overline{\mathbf{B}}] \\
&= \mathbf{K}_{uu} - \mathbf{K}_{uw}[\chi]([\chi]^T\mathbf{K}_{ww}[\chi])^{-1}[\chi]^T\mathbf{K}_{wu} \\
&\doteqdot \mathbf{K}_{uu} - \mathbf{K}_{uw}[_0\chi]([_0\chi]^T\mathbf{K}_{ww}[_0\chi])^{-1}[_0\chi]^T\mathbf{K}_{wu} \\
&= \mathbf{K}_{uu} - [\overline{\mathbf{B}}]^T[\chi]^T\mathbf{K}_{ww}[_0\chi] \\
&\quad \times([_0\chi]^T\mathbf{K}_{ww}[_0\chi])^{-1}[_0\chi]^T\mathbf{K}_{ww}[\chi][\overline{\mathbf{B}}] \\
&= \mathbf{K}_{uu} - \mathbf{K}_{u\alpha}\mathbf{K}_{\alpha\alpha}^{-1}\mathbf{K}_{\alpha u},
\end{aligned} \tag{80}$$

that is,

$$\begin{aligned}
&[\chi]^T\mathbf{K}_{ww}[\chi] \doteqdot [\chi]^T\mathbf{K}_{ww}[_0\chi] \\
&\times([_0\chi]^T\mathbf{K}_{ww}[_0\chi])^{-1}[_0\chi]^T\mathbf{K}_{ww}[\chi],
\end{aligned} \tag{81}$$

is employed. In the mode superposition method, since the homogenized tangent stiffness corresponds to the exact value with the mode updated at every Newton–Raphson iteration as described above, this method can give an approximate mean of the homogenized tangent stiffness by decreasing the number of times that the mode is updated. This method is referred to as the mode superposition algorithm (MSA).

4 Numerical examples

4.1 Comparison of computational costs and convergence properties

With respect to computational cost and convergence, which are of interest to us, we now compare the four methods introduced in the previous section, namely, the generalized algorithm (GA), block LU factorization algorithm (BFA), modified block LU factorization algorithm (MBFA) and the algorithm using mode superposition (MSA). Detailed algorithms for the parallel computation of each of the methods are given in Fig. 2. The GA calculates the microscopic equilibrium at each quadrature point in every iteration. In contrast to the GA, the BFA, MBFA, and MSA decrease the residual

1. Set calculation condition
2. Perform in a unit cell at each quadrature point by paraell computation
   Solve microscopic equilibrium problem : $\{\mathbf{r}_w\} = 0$
   Update the microscopic deformation : $\{\mathbf{w}\}$
   Solve for update χ : $\mathbf{K}_\chi[\chi^Q] = [\mathbf{r}_\chi]$
   Compute : $\mathbf{K}_{uu} - \mathbf{K}_{uw}\mathbf{K}_{ww}^{-1}\mathbf{K}_{wu}, \{\mathbf{r}_u\}$
3. Communication using MPIallreduce
   Assemble : $\mathbf{K}_{uu} - \mathbf{K}_{uw}\mathbf{K}_{ww}^{-1}\mathbf{K}_{wu}, \{\mathbf{r}_u\}$
4. Solve
   $$(\mathbf{K}_{uu} - \mathbf{K}_{uw}[\chi][\overline{\mathbf{B}}])\{\Delta\mathbf{u}\} = \{\mathbf{r}_u\}$$
5. Update the vatiables
   $$\{\mathbf{u}\} = \{\mathbf{u}\} + \{\Delta\mathbf{u}\}$$
6. if $|\{\mathbf{r}_u\}| < Tol$, then
   Next step GOTO 1
   else
   Next iteration GOTO 2

(a)

1. Set calculation condition
2. Perform in a unit cell at each quadrature point by paraell computation
   Compute : $\mathbf{K}_{ww}, \{\mathbf{r}_w\}$
   Solve : $\mathbf{K}_{ww}\{\Delta\tilde{\mathbf{w}}\} = \{\mathbf{r}_w\}$
   Update the microscopic deformation: $\{\mathbf{w}\} = \{\mathbf{w}\} + \{\Delta\tilde{\mathbf{w}}\}$
   In the BFA, everytime solve for update χ : $\mathbf{K}_\chi[\chi^Q] = [\mathbf{r}_\chi]$
   (In the MBFA, sometime solve for update χ_0 : $\mathbf{K}_\chi[\chi^Q] = [\mathbf{r}_\chi]$)
   Compute : $\mathbf{S}, \{\mathbf{r}_u\} - \mathbf{K}_{uw}\{\Delta\tilde{\mathbf{w}}\}$
3. Communication using MPIallreduce
   Assemble : $\mathbf{S}, \{\mathbf{r}_u\} - \mathbf{K}_{uw}\{\Delta\tilde{\mathbf{w}}\}$
4. Solve
   $$\mathbf{S}\{\Delta\mathbf{u}\} = \{\mathbf{r}_u\} - \mathbf{K}_{uw}\{\Delta\tilde{\mathbf{w}}\}$$
5. Update the vatiables
   $\{\mathbf{u}\} = \{\mathbf{u}\} + \{\Delta\mathbf{u}\}$
   In the BFA, $\{\mathbf{w}\} = \{\tilde{\mathbf{w}}\} - [\chi]\Delta\overline{\mathbf{F}}$
   In the MBFA, $\{\mathbf{w}\} = \{\tilde{\mathbf{w}}\} - [\chi_0]\Delta\overline{\mathbf{F}}$
6. if $|\{\mathbf{r}_w\}| < Tol, |\{\mathbf{r}_u\}| < Tol$, then
   Next step GOTO 1
   else
   Next iteration GOTO 2

(b)

1. Set calculation condition
2. Perform in a unit cell at each quadrature point by paraell computation
   Compute : $\mathbf{K}_{ww}, \{\mathbf{r}_w\}$
   Solve : $\mathbf{K}_{ww}\{\Delta\tilde{\mathbf{w}}\} = \{\mathbf{r}_w\}$
   Update the microscopic deformation: $\{\mathbf{w}\} = \{\mathbf{w}\} + \{\Delta\tilde{\mathbf{w}}\}$
   (Sometime solve for update χ_0 : $\mathbf{K}_\chi[\chi^Q] = [\mathbf{r}_\chi]$)
   Compute : $\mathbf{K}_{uu}, \mathbf{K}_{u\alpha}, \mathbf{K}_{\alpha u}, \mathbf{K}_{\alpha\alpha}, \{\mathbf{r}_\alpha\}, \{\mathbf{r}_u\}$
3. Communication using MPIallreduce
   Assemble : $\mathbf{K}_{uu}, \mathbf{K}_{u\alpha}, \mathbf{K}_{\alpha u}, \mathbf{K}_{\alpha\alpha}, \{\mathbf{r}_\alpha\}, \{\mathbf{r}_u\}$
4. Solve
   $$\begin{bmatrix}\mathbf{K}_{\alpha\alpha} & \mathbf{K}_{\alpha u}\\ \mathbf{K}_{u\alpha} & \mathbf{K}_{uu}\end{bmatrix}\begin{Bmatrix}\Delta\alpha\\ \Delta\mathbf{u}\end{Bmatrix} = \begin{Bmatrix}\mathbf{r}_\alpha\\ \mathbf{r}_u\end{Bmatrix}$$
5. Update the vatiables
   $$\{\mathbf{u}\} = \{\mathbf{u}\} + \{\Delta\mathbf{u}\}$$
   $$\{\alpha\} = \{\alpha\} + \{\Delta\alpha\}$$
   $$\{\mathbf{w}\} = \{\tilde{\mathbf{w}}\} - [_0\chi]\{\Delta\alpha\}$$
6. if $|\{\mathbf{r}_w\}| < Tol, |\{\mathbf{r}_u\}| < Tol$, then
   Next step GOTO 1
   else
   Next iteration GOTO 2

(c)

Fig. 2 Algorithms for parallel computation using the message passing interface (MPI). **a** Algorithms for GA. **b** Algorithms for BFA and MBFA. **c** Algorithms for MSA

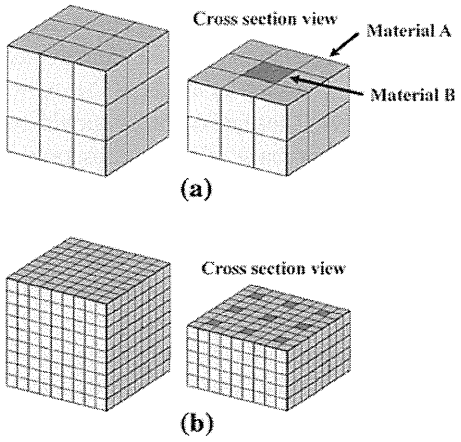

Fig. 3 FE models used in the calculation time evaluation. **a** 64 nodes, 27 elements (minimum size). **b** 1000 nodes, 729 elements

Table 1 Material constants for the models used in the calculation time evaluation

	E[kPa]	ν
Material A in Fig. 3	0.1	0.3
Material B in Fig. 3	10.0	0.3

of both scales simultaneously. Moreover, in the MBFA and MSA the straightforward update of S is avoided. We performed a 20% tensile test using the mesh of the block shown in Fig. 3 as the microstructure, and a single 8-node element as the macrostructure. The minimum size of the mesh is constructed from 27 ($3 \times 3 \times 3$) elements as shown in Fig. 3a, with the stiffness of the center element different from the rest.

The NDOF is adjusted by adding the same number of minimum units in each direction (e.g. Fig. 3b). The St. Venant hyperelastic material is used for the constitutive equations

$$W = \frac{1}{2}\lambda(tr\mathbf{E})^2 + \mu\mathbf{E} : \mathbf{E}, \tag{82}$$

$$\mathbf{S} = \frac{\partial W}{\partial \mathbf{E}} = (\lambda\mathbf{I} \otimes \mathbf{I} + 2\mu\mathbf{I}) : \mathbf{E} = \mathbf{C} : \mathbf{E}, \tag{83}$$

$$l_{ijkl} = \delta_{ik}\delta_{jl}, \tag{84}$$

$$\lambda = \frac{E\nu}{(1+\nu)(1-2\nu)}, \quad \mu = G = \frac{E}{2(1+\nu)}, \tag{85}$$

where $\mathbf{I}$ is a second order identity tensor, λ and μ are Lame constants, and E and ν are, respectively, Young's modulus and Poisson's ratio. $\mathbf{C}$ is a fourth order constant elasticity tensor and the relationship between $\boldsymbol{S}$ and $\boldsymbol{E}$ is linear. The material constants are given in Table 1. If the material constants are assumed to be uniform in the microstructure, the solutions obtained by these methods agree completely with the theoretical solution in the case of infinitesimal deformation. We have thus confirmed the correctness of the formulations

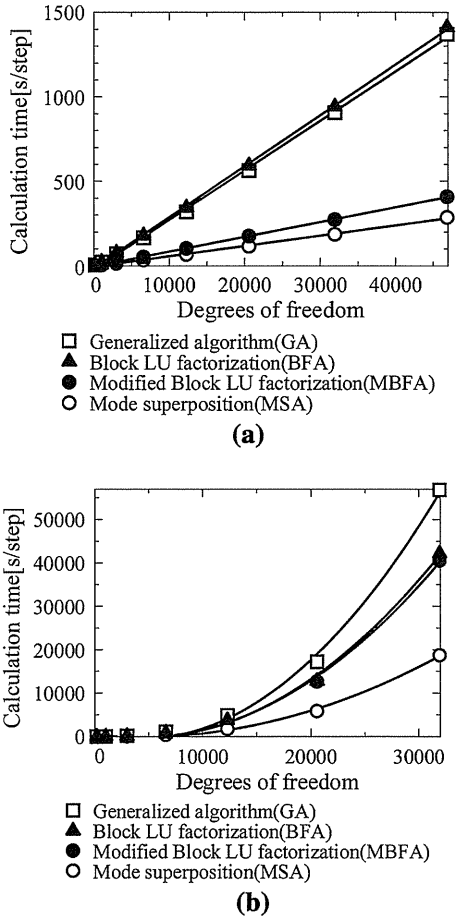

Fig. 4 Comparison of calculation time. **a** Iterative solver. **b** Direct solver

and computer programs. The relationship between calculation time and NDOF of the microstructure for each algorithm is depicted in Fig. 4 for cases where an iterative solver (ILU preconditioned GMRES method) or direct solver (skyline method) are used. The breakdown of calculation time and number of iterations in each process, where the NDOF of the microstructure is 31,944, are given in Table 2. Convergence is judged to occur when the root sum square reaches 1×10^{-10} times the initial value. As shown in Fig. 4, the calculation time of the BFA using an iterative solver slightly exceeds that of the GA. In the BFA, equilibrium of the microstructure is not required within an iteration for the sake of computational efficiency, but this may result in more iterations compared with the GA. Table 2 illustrates this, in that the BFA requires 5 iterations whereas the GA requires 4. We need to calculate the characteristic deformation to update the Schur-Complement; this means that the nine different right-hand sides of Eq. (33) must be solved in the case of the iterative solver. Consequently, the increased number of iterations results in a deterioration in the performance of the BFA. If a direct solver is used instead, the result of the LU decomposition

Table 2 Calculation time and number of iterations in each process

	Calculation of χ (s)	Calculation of equilibrium in the microscopic model (s)	Total (s)	No. of iterations
a. Iterative solver				
GA	670	211	906	4
BFA	805	107	942	5
MBFA	17	195	273	11
MSA	21	113	186	5
b. Direct solver				
GA	19,816	36,949	56,791	4
BFA	23,689	18,492	42,212	5
MBFA	451	40,050	40,557	11
MSA	457	18,237	18,746	5

of the stiffness matrix can be reused in the computation of the characteristic deformation, and as a result, the computational cost of the BFA is 20% less than that of the GA, despite the BFA using one more iteration than the GA. On the other hand, the MBFA is much faster than both the BFA and the GA when an iterative solver is used, although in the case of a direct solver there is almost no difference between the MBFA and BFA. This is because the calculation cost of the mode update in the BFA is similar to that of the increased iterations in the MBFA. However, convergence in the MBFA is slow as shown in Fig. 5 and it is anticipated that for strong nonlinear problems, convergence may not be achieved at all. Here, the characteristic deformation was approximated by that obtained at the beginning of the analysis. Convergence can be improved by incorporating more frequent updates, at the expense of CPU time. Compared with these methods, the MSA always exhibits excellent speed and convergence. The advantage of the MSA is twofold. First, the approximation of the Schur-Complement is more accurate than in the MBFA, i.e., Eq. (80) gives a superior approximation than Eq. (72). Second, in an iteration of the MSA, the microscopic equation is solved in Eq. (75) in terms of $\Delta\alpha$ as well as in Eq. (74) with Eq. (69). These advantages should contribute to an accelerated convergence of the microscopic equation as well as the macroscopic equation. Although the St. Venant hyperelastic material assumed here has relatively weak nonlinearity, the number of iterations does not increase up to a large deformation range, even with the initial characteristic deformation being used for ${}_0\chi$. However, a periodic update of ${}_0\chi$ is required in the case of strong nonlinear material, such as an elasto-plastic material. If ${}_0\chi$ is updated at every iteration, the homogenized tangent stiffness corresponds to the exact value as described in Eq. (80).

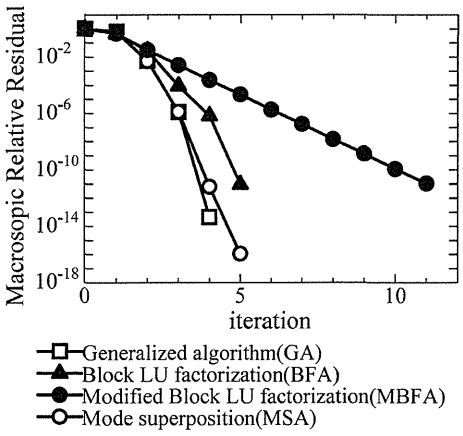

Fig. 5 Comparison of convergence property

4.2 Application to ventricle–cardiomyocyte analysis with parallel computation

As seen in Table 2, most of the calculation cost relates to the microscopic equilibrium (Eq. (69)) when the MBFA or MSA is used. In addition, as the NDOF of the microscopic model becomes larger, the computational cost for the macroscopic model becomes more negligible. It is therefore crucial to decrease the time for microscopic calculation in real problems. Since Eq. (69) holds independently at each macroscopic quadrature point, parallel computation is effective in the homogenization method. In other words, microscopic models can be distributed equally to the available cores, and this directly accelerates the microscopic calculation according to the number of cores. Moreover, since the memory is shared by fewer microscopic models in the parallel computation, a greater NDOF of the microstructure can be handled.

Figures 6 and 7 show a simplified human cardiomyocyte–ventricle model, to which we have applied the MSA. As shown on the left and in the center of Fig. 7 a simplified cardiomyocyte model is constructed with extracellular and intracellular matrices and gap junctions. The total NDOF is 20385. If the models are arrayed periodically in the three directions as depicted on the right of the figure, a fairly accurate imitation of a microgram of real tissue is obtained. The

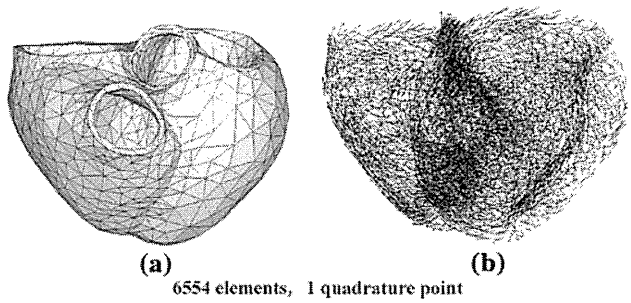

Fig. 6 FE meshes of ventricles as macroscopic model. **a** FE mesh. **b** Fiber orientation

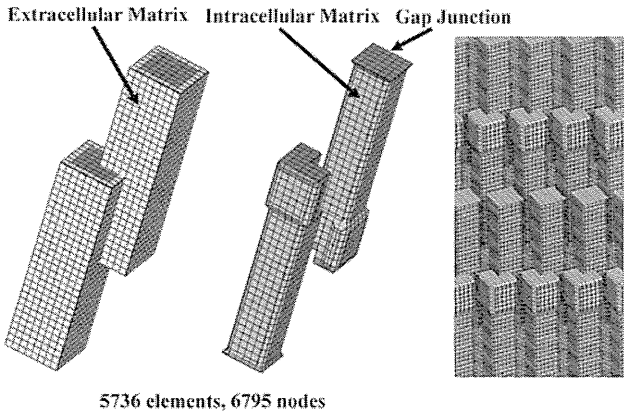

Fig. 7 FE meshes of cardiomyocytes as microscopic model

Table 3 Material constants for the cell model

	C_1	C_2	κ
Gap Junction	1×10^5	1×10^5	2×10^5
Intracellular Matrix	1×10^4	1×10^4	2×10^4
Extracellular Matrix	1×10^3	1×10^3	2×10^3

Mooney–Rivlin material using reduced invariants is adopted for the constitutive equation, with the material constants listed in Table 3.

$$W = C_1(\tilde{I}_c - 3) + C_2(\tilde{II}_c - 3) + \frac{\kappa}{2}U^2 \tag{86}$$

$$\tilde{I}_c = \frac{I_c}{III_c^{1/3}}, \quad \tilde{II}_c = \frac{II_c}{III_c^{2/3}} \tag{87}$$

$$U = J - 1, \tag{88}$$

where U is the volumetric strain energy function and κ is the bulk modulus. The ventricle model is constructed based on CT imaging, with fiber directions distributed from -90 to 60 degrees, relative to the plane perpendicular to the long axis of the ventricle. The fiber direction denotes the long axis (z-axis) of the cardiomyocyte model, and therefore, proper rotation is taken into consideration for each micromodel. In this model, the intracellular matrix is defined as a function of a parameter that represents the excitation of the myocyte, and this parameter is varied at every time step to represent the transient contraction force. The homogenization method is applied to 6,554 elements covering the greater region of the ventricle, whereas the conventional Mooney–Rivlin hyperelastic constitutive law is assumed for the limited regions at the base and apex. To reduce the computational cost, a single myocyte (micromodel) is assigned to each finite element of the ventricle, i.e., 6,554 cardiomyocyte models are embedded in the ventricle model. The total NDOF, including those of the ventricles, amounts to 133,609,263.

The computer used was an IBM Blade Center consisting of 336 Power6 (4.0 GHz) processors. Considering the size of

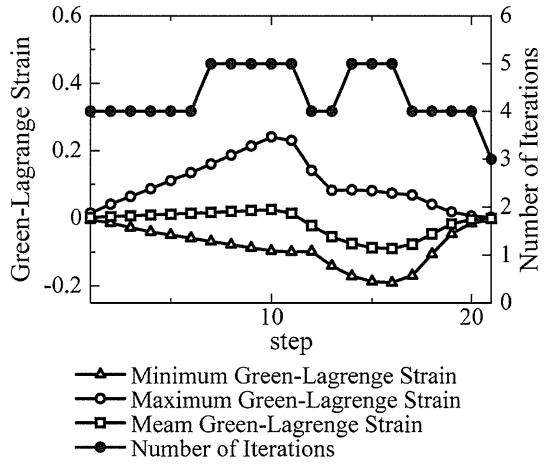

Fig. 8 Green–Lagrenge strains and nunber of iterations at each step

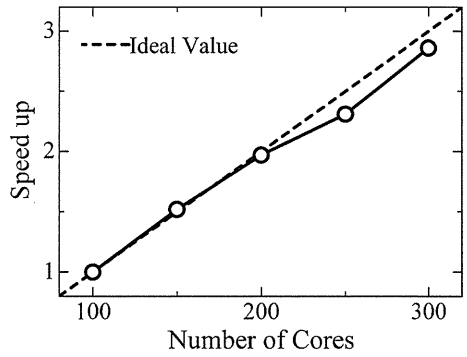

Fig. 9 Speed up in parallel computation

the problem, convergence was deemed to occur when the root sum square of the macro and micro residuals was 1×10^{-5} times less than the initial value. Figure 8 shows the maximum, the minimum and the mean Green–Lagrange strains throughout the ventricle model, and the number of iterations of the MSA at each time step. The strains are measured in the fiber direction. Although the maximum and the minimum strains reach $\pm 20\%$, an excellent convergence property was observed. Figure 9 shows the resulting scalability, by depicting the speed up rate relative to a hundred-core computation. As shown in this figure, satisfactory parallel performance was obtained by the proposed algorithm. The deformations of the ventricle and a representative myocyte in the diastole and the systole are exemplified in Fig. 10. The CPU time for the completion of a cardiac cycle was about 24 h when using 300 cores. The proposed method thus allows us to deal with large-scale problems.

5 Conclusion

To reduce the computational cost of the nonlinear homogenization method, the theoretical framework was reassessed

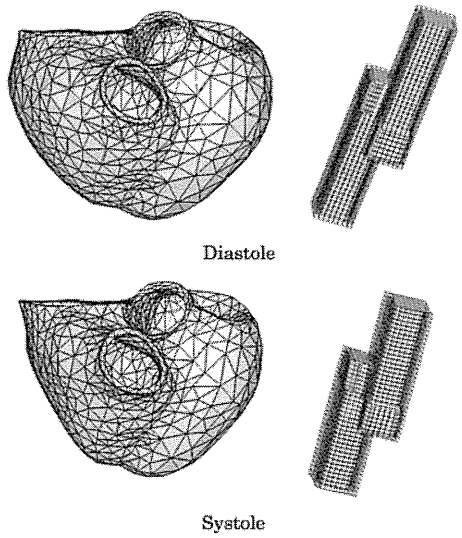

Fig. 10 Deformations of macro and microstructures in diastole and systole

from the perspective of block LU factorization of the micro–macro coupled equation. Based on the relation between the characteristic deformation and the Schur-Complement as the homogenized tangent stiffness, a couple of approximation methods were introduced, namely, a simple scheme to reuse the old characteristic deformation (MBFA) and a sophisticated method based on the mode-superposition method (MSA) developed by our group. It is noted that accuracy is preserved in these approximation methods by incorporating the equilibrium conditions in both scales. Then, using a simplified FE model, the conventional algorithm (GA), a relative algorithm originating from the block LU factorization (BFA), the MBFA, and the MSA were compared and discussed. Of these methods, the MSA was found to be the best. Then, using the MSA, a large-scale human ventricle–cardiomyocyte simulation was performed on an IBM Blade Center consisting of 336 Power6 processors, and good parallel performance was demonstrated. We plan to use the proposed homogenization algorithm in a whole-heart simulation on a massively parallel computer in the near future.

Acknowledgments Our current research on homogenization method stems from Reference [10] coauthored by Hirohisa Noguchi. We again recognize his enthusiasm and contribution in a broad range of computational mechanics. This work was supported by Core Research for Evolutional Science and Technology, Japan Science and Technology Agency.

References

1. Terada K, Hori M, Kyoya T, Kikuchi N (2000) Simulation of the multi-scale convergence in computational homogenization approaches. Int J Solids Struct 37:2285–2311
2. Hollister SJ, Kikuchi N (1992) Comparison of homogenization and standard mechanics analyses for periodic porous composites. Comput Mech 10:73–95
3. Breuls RGM, Sengers BG, Oomens CWJ, Bouten CVC, Baaijens FPT (2002) Predicting local cell deformations in engineered tissue constructs: a multilevel finite element approach. ASME J Biomech Eng 124:198–207
4. Krassowska W, Pilkington TC, Ideker RE (1990) Potential distribution in three-dimensional periodic myocardium: Part I. Solution with two-scale asymptotic analysis. IEEE Trans Biomed Eng 37:252–266
5. Terada K, Kikuchi N (2001) A class of general algorithms for multi-scale analyses of heterogeneous media. Comput Methods Appl Mech Eng 190:5427–5464
6. Matsui K, Terada K, Yuge K (2004) Two-scale finite element analysis of heterogeneous solids with periodic microstructures. Comput Struct 82:593–606
7. Takano N, Ohnishi Y, Zako M, Nishiyabu K (2001) Microstructure-based deep-drawing simulation of knitted fabric reinforced thermoplastics by homogenization theory. Int J Solids Struct 38:6333–6356
8. Rohan E (2003) Sensitivity strategies in modelling heterogeneous media undergoing finite deformation. Math Comput Simul 61:261–270
9. Moulinec H, Suquet P (1998) A numerical method for computing the overall response of nonlinear composites with complex microstructure. Comput Methods Appl Mech Eng 157:69–94
10. Yamamoto M, Hisada T, Noguchi H (2001) Homogenization method for large deformation problem by using characteristic deformation mode superposition. Trans Jpn Soc Mech Eng 67:1877–1884 (in Japanese)
11. Yamamoto M, Hisada T (2002) A homogenization method for nearly incompressible materials by using characteristic deformation mode superposition. Trans Jpn Soc Mech Eng A 45:596–602
12. Okada J, Hisada T (2006) Homogenization method for mixed finite element analysis of incompressible hyper-elastic materials. In: JSCES e06: Proceedings of the 11th computational engineering conference, Osaka, Japan, pp 79–82 (in Japanese)
13. Okada J, Hisada T (2006) Homogenization method for mixed finite element analysis of incompressible viscoelastic materials. In: Proceedings of the 19th JSME computational mechanics conference, Nagoya, Japan, pp 45–46 (in Japanese)
14. Okada J, Hisada T (2009) Study on compressibility control of hyperelastic material for homogenization method using mixed finite element analysis. J Comput Sci Technol 3(1):89–100
15. Okada J, Washio T, Hisada T (2009) Nonlinear homogenization algorithms with low computational cost. J Comput Sci Technol 3(1):101–114
16. Miehe C, Schroder J, Schotte J (1999) Computational homogenization analysis in finite plasticity. Simulation of texture development in polycrystalline materials. Comput Methods Appl Mech Eng 171:387–418
17. Allaire G (1992) Homogenization and two-scale convergence. SIAM J Math Anal 23:1482–1518
18. Terada K, Kikuchi N (2003) Introduction to the method of homogenization. Maruzen (in Japanese)
19. Yamada T, Matsui K (2007) Numerical procedure for nonlinear multiscale problems based on block Newton method. Proc Conf Comput Eng Sci 12:309–312 (in Japanese)

Artificial Organs

Artificial Organs
33(9):767–773, Wiley Periodicals, Inc.

Thoughts and Progress

Baroreflex Sensitivity of an Arterial Wall During Rotary Blood Pump Assistance

*Tomoyuki Yambe, *Kou Imachi, *Yasuyuki Shiraishi, †Tasuku Yamaguchi, ‡Mune-ichi Shibata, §Takeshi Kameyama, **Makoto Yoshizawa, and **Norihiro Sugita
*Department of Medical Engineering and Cardiology, Institute of Development, Aging and Cancer, Tohoku University, †Tohoku Kouseinenkin Hospital, ‡Miyagi Prefectural Cardio-respiratory Center, §Miyagi Shakaihoken Hospital, **Information Synergy Center, Tohoku University, Tohoku, Japan

Abstract: It is well known that the baroreflex system is one of the most important indicators of the pathophysiology in hypertensive patients. We can check the sensitivity of the baroreflex by observing heart rate (HR) responses; however, there is no simple diagnostic method to measure the arterial behavior in the baroreflex system. Presently, we report the development of a method and associated hardware that enables the diagnosis of baroreflex sensitivity by measuring the responses of both the heart and the artery. In this system, the measurements are obtained by monitoring an electrocardiogram and a pulse wave recorded from the radial artery or fingertip. The arterial responses were measured in terms of the pulse wave velocity (PWV) calculated from the pulse wave transmission time (PTT) from the heart to the artery. In this system, the HR change corresponding to the blood pressure change in time series sequence was observed. Slope of the changes in blood pressure and HR indicated the sensitivity of the baroreflex system of the heart. This system could also measure the sensitivity of the baroreflex system of an artery. Changes in the PWV in response to the blood pressure changes were observed. Significant correlation was observed in the time sequence between blood pressure change and PWV change after calculating the delay time by cross-correlation. The slope of these parameter changes was easily obtained and it demonstrated the sensitivity of the baroreflex system of an artery. We evaluated this method in animal experiments using rotary blood pump (RBP) with undulation pump ventricular assist device, and PTT elongation was observed in response to increased blood pressure with RBP assistance. Furthermore, when tested clinically, decreased sensitivity of the baroreflex system in hypertensive patients was observed. This system may be useful when we consider the ideal treatment and follow-up of patients with hypertension. **Key Words:** Baroreflex sensitivity—Arterial baroreflex—Baroreceptor—Pulse wave transmission time—Pulse wave velocity—Rotary blood pump.

doi:10.1111/j.1525-1594.2009.00864.x

Received December 2008; revised March 2009.

Address correspondence and reprint requests to Dr. Tomoyuki Yambe, 4-1 Seiryo-machi, Aoba-ku, Sendai 980-8575, Japan. E-mail; yambe@idac.tohoku.ac.jp

Presented in part at the 16th Congress of the International Society for Rotary Blood Pumps held Oct. 2–4, 2008 in Houston, TX, USA.

The baroreflex system is a key indicator of hypertensive pathophysiology (1–4). When blood pressure (BP) increases, heart rate (HR) decreases, and there is peripheral arterial dilation (1–6). By decreasing the cardiac output and peripheral arterial resistance, BP returns to normal. Hypertension is a concern in the young as well as the elderly (4–6). Baroreflex sensitivity is reduced in younger hypertensive patients (4–6). However, currently there is no simple and sensitive diagnostic method to measure the arterial behavior in the baroreflex system.

Both responses of the HR and vasomotor components are important when we consider the precise quantitative diagnosis of the autonomic nervous system mediating the baroreflex system in the human body. However no one has reported the methodology to evaluate the vasomotor components in the baroreflex system. No report describing the baroreflex sensitivity in vasomotor components can be cited currently according to PubMed. So, we cannot evaluate the importance of the HR in baroreflex sensitivity, because we cannot evaluate the vasomotor components.

Several investigators suggested the regional differentiation in autonomic responses in various human body areas. So, we cannot evaluate total response of the baroreflex system by only observing the HR. It may be a disadvantage if we cannot evaluate the precise quantification of the baroreflex system. Precise evaluation may be clearly desirable when we consider the ideal treatment and follow-up of patients with hypertension.

This study describes the development and clinical application of a new novel baroreflex diagnostic machine and offers a preliminary consideration of its clinical applicability in patients with rotary blood pump assistance.

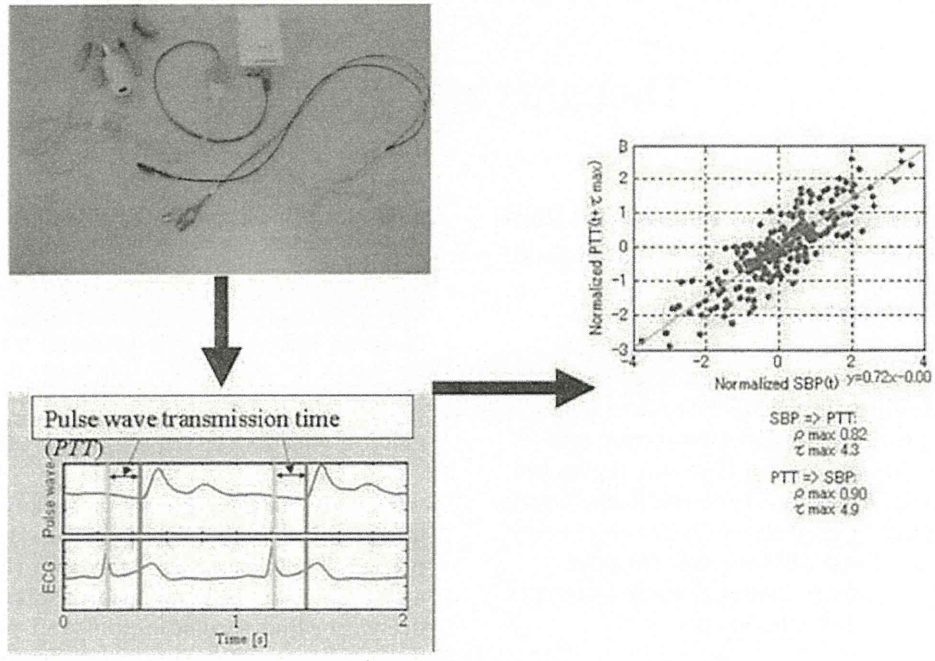

FIG. 1. Schematic diagram to explain the PWV and PTT. A photograph of the measurement equipment is shown on the upper left side. By the use of the ECG and finger tip artery waveform, we can calculate the PTT from R wave in ECG and rising point of radial arterial pressure waveform. An example of the correlation between the normalized systolic BP and normalized PTT in a patient is shown on the right. Significant correlation was observed, and the slope, suggesting the baroreflex sensitivity of an arterial tree, was calculated from the regression line from least square method.

DIAGNOSIS OF ARTERIAL BAROREFLEX SENSITIVITY

Every medical student studies the baroreflex system as a typical example of homeostasis (1–6). When BP increases, baroreceptors in the carotid arteries and aortic arch sense this. The carotid sinus baroreceptors are innervated by the glossopharyngeal nerve, the aortic arch baroreceptors are innervated by the vagus nerve. With information transmitting to the central nervous system, the HR lowers and arteries dilate by coupling sympathetic inhibition and parasympathetic activation.

In the conventional method, the baroreflex sensitivity was evaluated by measuring the HR response to the BP changes. Although HR response in the baroreflex system can be monitored, no method currently exists to evaluate arterial baroreflex function, possibly because of the difficulty in evaluating vascular tone during wakefulness.

Recently, new methodologies like brachial-ankle pulse wave velocity (baPWV) have been developed to evaluate human arterial stiffness (7–10). These methodologies non-invasively evaluate arterial wall stiffness using the pulse waveform of the brachial and ankle arteries. These methodologies are based on the premise that PWV is correlated with arterial wall stiffness. Thus, PWV increases when the arterial wall becomes harder and decreases when the arterial wall softens. PWV can be calculated from the pulse wave transmission time (PTT) and distance (Fig. 1). Thus, measurements of PTT and BP permit an evaluation of arterial baroreflex response. Time was calculated from the R wave in the electrocardiogram (ECG) and upsloping point of pressure waveform.

PTT and PWV were easily measured by monitoring ECG and pulse wave. Figure 1 shows the equipment used for the measurement. The newly developed system used only an ECG and a pulse wave recorded from the radial artery. These time series were inputted into a personal computer, and analyzed quantitatively using custom-developed software. HR was calculated from the reciprocal of the inter-R-wave interval of the ECG signal. PTT was defined as the time interval from the peak of the R wave to the point at which the pulse wave signal began to increase. HR and PTT were interpolated by cubic spine functions to continuous-time functions, and were resampled every 0.5 s.

The right side of Fig. 1 displays an example of the correlation between the systolic BP and

PTT. PTT was plotted after 6.0 s. Significant correlation was evident in the time sequence between BP change and PTT change after calculating the delay time by cross-correlation. The slope of these parameter changes was easily obtained, and it demonstrated the sensitivity of the baroreflex system of an artery.

The utility of this system for the quantitative diagnosis of the baroreflex sensitivity of an artery was recognized by the patent application.

UNDULATION PUMP VENTRICULAR ASSIST DEVICE (UPVAD) AND PTT CHANGE IN RESPONSE TO BP CHANGE

On the basis of this method, rotary blood pump with undulation pump was used in experiments to evaluate the arterial response to the rotary blood pump assistance (11,12). A healthy adult goat with UPVAD rotary blood pump was used in this experiment and results are shown in Fig. 2. If we added the rotary blood pump assistance, BP was increased and the PTT was increased in response. However, the results were influenced by the HR, of course. So, we added the pacemaker on this experiment and the results are shown in Fig. 2. During pacing, PTT was also increased in response to BP change with RBP assistance.

So, this information is also useful when we consider the hemodynamics with RBP assistance.

CONCLUSIONS

The arterial responses were measured in terms of the PWV calculated from the PTT from the heart to an artery (13,14). In this system, the HR change corresponding to the BP change in time series sequence was observed. Delay time was measured by the cross-correlation function. Slope of the changes in BP and HR indicates the sensitivity of the baroreflex system of heart. Furthermore, this system could also measure the sensitivity of the baroreflex system of an artery.

Clinical research of our study has begun after ethical committee allowance. So far, the results have shown that our system can successfully detect decreased sensitivity of the baroreflex system in hypertensive patients. We are now analyzing the various data of the patients with hypertension by gathering data from related hospitals.

Further examination will be needed using more cases. This new method may be useful to follow up patients with hypertension.

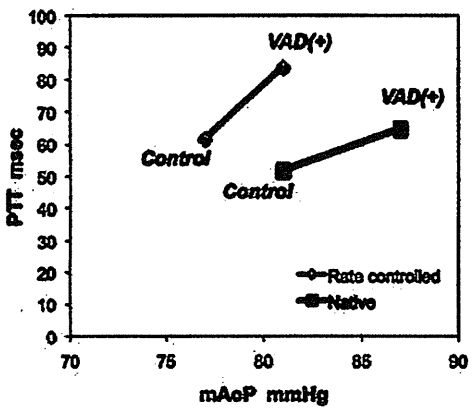

FIG. 2. An example of a PTT response to the rotary blood pump assistance with and without pacemaker. If we added the rotary blood pump assistance with UPVAD, BP was increased and the PTT was increased in response. However, the results were influenced by the HR, of course. So, we added the pacemaker on this experiment. During pacing, PTT was also increased in response to BP change with RBP assistance.

Acknowledgements: This work was partly supported by the support of Tohoku University Global COE Program "Global Nano-Biomedical Engineering Education and Research Network Centre" and research grants from Mitsui Sumitomo Insurance Welfare Foundation, Nakatani Electronic Measuring Technology Association of Japan, Japan Epilepsy Research Foundation, and the Naito Foundation.

REFERENCES

1. Grassi G, Dell'Oro R, Quarti-Trevano F, et al. Neuroadrenergic and reflex abnormalities in patients with metabolic syndrome. *Diabetologia* 2005;48:1359–65.
2. Chen HI. Mechanism of alteration in baroreflex cardiovascular responses due to volume loading. *Jpn J Physiol* 1978;28: 749–56.
3. Goldstein DS, Harris AH, Brady JV. Baroreflex sensitivity during operant blood pressure conditioning. *Biofeedback Self Regul* 1977;2:127–38.
4. Krontoradova K, Honzikova N, Fiser B, et al. Overweight and decreased baroreflex sensitivity as independent risk factors for hypertension in children, adolescents, and young adults. *Physiol Res* 2007;May 30 (Epub ahead of print).
5. Fu Q, Townsend NE, Shiller SM, et al. Intermittent hypobaric hypoxia exposure does not cause sustained alterations in autonomic control of blood pressure in young athletes. *Am J Physiol Regul Integr Comp Physiol* 2007;292:R1977–84. Epub 2007 Jan 4.
6. Honzikova N, Novakova Z, Zavodna E, et al. Baroreflex sensitivity in children, adolescents, and young adults with essential and white-coat hypertension. *Klin Padiatr* 2006;218:237–42.
7. Yambe T, Kovalev YA, Milyagina IA, et al. Japanese-Russian collaborative study on aging and atherosclerosis. *Biomed Pharmacother* 2004;58:S91–4.
8. Yamashina A, Tomiyama H, Arai T, et al. Nomogram of the relation of brachial-ankle pulse wave velocity with blood pressure. *Hypertens Res* 2003;26:801–6.
9. Yambe T, Meng X, Hou X, et al. Cardio-ankle vascular index (CAVI) for the monitoring of the atherosclerosis after heart transplantation. *Biomed Pharmacother* 2005;59:S177–9.

10. Yambe T, Yoshizawa M, Saijo Y, et al. Brachio-ankle pulse wave velocity and cardio-ankle vascular index (CAVI). *Biomed Pharmacother* 2004;58:S95–8.
11. Yambe T, Abe Y, Imachi K, et al. Development of an implantable undulation type ventricular assist device for control of organ circulation. *Artif Organs* 2004;28:940–4.
12. Abe Y, Isoyama T, Saito I, et al. Development of mechanical circulatory support devices at the University of Tokyo. *J Artif Organs* 2007;10:60–70.
13. Yambe T, Shiraishi Y, Saijo Y, et al. Quantitative evaluation of the baroreflex sensitivity of an artery. *Scripta Medica* 2008; 81:249–60.
14. Liu H, Saijo Y, Zhang X, et al. Impact of type A behavior on brachial-ankle pulse wave velocity in Japanese. *Tohoku J Exp Med* 2006;209:15–21.

31st Annual International Conference of the IEEE EMBS
Minneapolis, Minnesota, USA, September 2-6, 2009

Estimation of Blood Pressure Variability Using Independent Component Analysis of Photoplethysmographic Signal

Makoto Abe, *Member, IEEE*, Makoto Yoshizawa, *Member, IEEE*, Norihiro Sugita, Akira Tanaka, *Member, IEEE*, Shigeru Chiba, Tomoyuki Yambe and Shin-ichi Nitta

Abstract— **The maximum cross-correlation coefficient $\rho_{\max}$ between blood pressure variability and heart rate variability, whose frequency components are limited to the Mayer wave-related band, is a useful index to evaluate the state of the autonomic nervous function related to baroreflex. However, measurement of continuous blood pressure with an expensive and bulky measuring device is required to calculate $\rho_{\max}$. The present study has proposed an easier method for obtaining $\rho_{\max}$ with measurement of finger photoplethysmography (PPG). In the proposed method, independent components are extracted from feature variables specified by the PPG signal by using the independent component analysis (ICA), and then the most appropriate component is chosen out of them so that the $\rho_{\max}$ based on the component can fit its true value. The results from the experiment with a postural change performed in 17 healthy subjects suggested that the proposed method is available for estimating $\rho_{\max}$ by using the ICA to extract blood pressure information from the PPG signal.**

I. INTRODUCTION

To estimate the state of the autonomic nervous system related to the baroreflex function, the authors have previously proposed the maximum cross-correlation coefficient $\rho_{\max}$ between blood pressure variability (BPV) and heart rate variability (HRV) in Mayer wave band [1][2]. However, measurement of continuous blood pressure is required to obtain $\rho_{\max}$. Instead of blood pressure, we have attended to measurement of photoplethysmography (PPG) which is an inexpensive, non-invasive, and easily attachable device. The index $\rho_{\max}$ obtained from a feature variable of PPG includes some physiological components other than BPV [3]. Thus, $\rho_{\max}$ obtained from feature variables of PPG does not always correspond to $\rho_{\max}$ from BPV. Therefore, in this study, we have proposed a new method for obtaining $\rho_{\max}$ with BPV-related information obtained from measurement of PPG. In this study, heart rate is calculated from the foot-to-foot-interval (FFI) of the PPG signal, and BPV-related information is obtained from the parameter extracted by using the independent component analysis (ICA). The adequacy of the proposed method was evaluated on the basis of comparison with the conventional method.

M. Abe and M. Yoshizawa are with the Research Division on Advanced Information Technology, Cyberscience Center, Tohoku University, 6-6-05 Aoba, Aramaki, Aoba-ku, Sendai 980-8579, Japan (corresponding author to provide phone: +81-22-795-7130; fax +81-22-263-9163; e-mail: abe@yoshizawa.ecei.tohoku.ac.jp).

N. Sugita is with Graduate School of Engineering, Tohoku University, 6-6-05 Aoba, Aramaki, Aoba-ku, Sendai 980-8579, Japan.

A. Tanaka is with Faculty of Symbiotic Systems Science, Fukushima University, 1 Kanayagawa, Fukushima 960-1296, Japan.

S. Chiba is with Sharp Corporation, 1-9-2 Nakase, Mihama-ku, Chiba 261-8520, Japan.

T. Yambe and S. Nitta are with Institute of Development, Aging and Cancer, Tohoku University, 4-1 Seiryo-cho, Aoba-ku, Sendai 980-8575, Japan.

II. METHODS

A. Maximum cross-correlation coefficient $\rho_{\max}$

Let $u(i)$ and $v(i); i = 0, 1, 2, \ldots$ denote time series data, for example, blood pressure variability (BPV) and heart rate variability (HRV), respectively, sampled with a sampling period $\Delta t = 0.5$s. They are filtered through a band-pass digital filter with a bandwidth between 0.08Hz and 0.12Hz to limit their frequency components to the Mayer wave band. At a certain time point $t = i \cdot \Delta t$[s], a Hamming window with the interval between $t - 60$[s] and $t + 60$[s] is applied to $u(i)$ and $v(i)$. A cross-correlation coefficient $\rho_{uv}(\tau)$ for a lag of $\tau = j \cdot \Delta t$[s]; $j = \ldots, -1, 0, 1, \ldots$ is calculated as follows:

$$\rho_{uv}(\tau) = \frac{\phi_{uv}(\tau)}{\sqrt{\phi_{uu}(0) \cdot \phi_{vv}(0)}} \tag{1}$$

where, $\phi_{uv}(\tau)$ is a cross-correlation function between $u(i)$ and $v(i)$, and $\phi_{uu}(\tau)$ and $\phi_{vv}(\tau)$ are auto-correlation functions of $u(i)$ and $v(i)$, respectively. The maximum cross-correlation coefficient $\rho_{\max}$ and the lag from BPV to HRV $\tau_{\max}$ are defined as

$$\rho_{\max} = \max_{0\text{s} \le \tau \le 10\text{s}} \rho_{uv}(\tau) \tag{2}$$

$$\tau_{\max} = \arg \max_{0\text{s} \le \tau \le 10\text{s}} \rho_{uv}(\tau). \tag{3}$$

In the present study, $\rho_{\max}$ is successively calculated every one second between $t = 60$[s] and $t = T - 60$[s], where T[s] is the end time of the data obtained from an experiment.

B. Independent component analysis (ICA)

The ICA used in our method is described as follows:

1) Let $x_1(k), x_2(k), \ldots, x_m(k)$ be m feature variables extracted from the PPG signal at the k-th beat. Define a feature vector $\boldsymbol{x}(k)$ as $\boldsymbol{x}(k) = [x_1(k), x_2(k), \ldots, x_m(k)]^{\mathrm{T}}$.
2) Let $s_1(k), s_2(k), \ldots, s_n(k)$ be n unknown physiological parameters that are independent of one another at the k-th beat. Define a parameter vector $\boldsymbol{s}(k)$ as $\boldsymbol{s}(k) = [s_1(k), s_2(k), \ldots, s_n(k)]^{\mathrm{T}}$.
3) Assume that the feature vector $\boldsymbol{x}(k)$ is given by a linear combination of $s_1(k), s_2(k), \ldots, s_n(k)$ as follows:

$$\boldsymbol{x}(k) = \boldsymbol{A}\boldsymbol{s}(k) \tag{4}$$

where, an $m \times n$ matrix $\boldsymbol{A}$ represents an unknown constant mixing matrix consisting of coefficients of the liner combination. Let K be the number of beats observed in an experiment. Define an $m \times K$ matrix $\boldsymbol{X}$ and an $n \times K$ matrix $\boldsymbol{S}$ as $\boldsymbol{X} = [\boldsymbol{x}(1), \boldsymbol{x}(2), \ldots, \boldsymbol{x}(K)]$ and $\boldsymbol{S} = [\boldsymbol{s}(1), \boldsymbol{s}(2), \ldots, \boldsymbol{s}(K)]$, respectively. Thus, the matrix $\boldsymbol{X}$ is assumed to be given by $\boldsymbol{S}$ as follows:

$$\boldsymbol{X} = \boldsymbol{A}\boldsymbol{S} \tag{5}$$

4) The ICA is applied to estimate the mixing matrix $\boldsymbol{A}$ from the matrix $\boldsymbol{X}$. The independent component $\boldsymbol{S}$ can be obtained by

$$\boldsymbol{S} = \boldsymbol{A}^{+}\boldsymbol{X} \tag{6}$$

where $\boldsymbol{A}^{+}$ is the pseudoinverse matrix of $\boldsymbol{A}$.

In this study, the fast fixed point algorithm (fast-ICA) presented by Hyvärinen and Oja was used to linearly separate $\boldsymbol{S}$ from $\boldsymbol{X}$ [4], [5]. Principal component analysis was used as a preprocessing of the ICA. Furthermore, the number of feature variables, m, was empirically set to 7 on the basis of the variables related to BP.

Figure 1 shows an example of the PPG signal. In this figure, 7 feature variables used in the present study are illustrated. These are defined every beat as follows:

1) FFI: the foot-to-foot interval of PPG
2) t_{d}: the interval from the time maximizing the PPG to the time minimizing PPG
3) t_{maxslope}: the time maximizing the slope of PPG
4) PW_{bias}: the minimum value of PPG
5) PW_{max}: the maximum value of PPG
6) DPW_{max}: the value of PPG at t_{maxslope}
7) $NPWA$: the area of PPG normalized by FFI

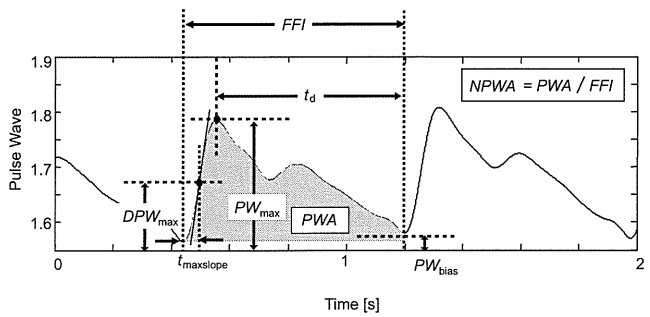

Fig. 1. Definition of feature variables.

These parameters include information on hemodynamic state such as blood pressure, blood volume, and vascular compliance. For example, the parameter $NPWA$ shows the mean value of the pulsatile component of arterial blood volume and is a candidate of substitutes of BPV.

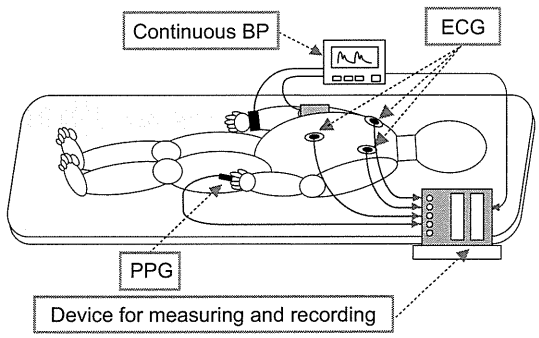

Fig. 2. Setup of experiment with supine posture

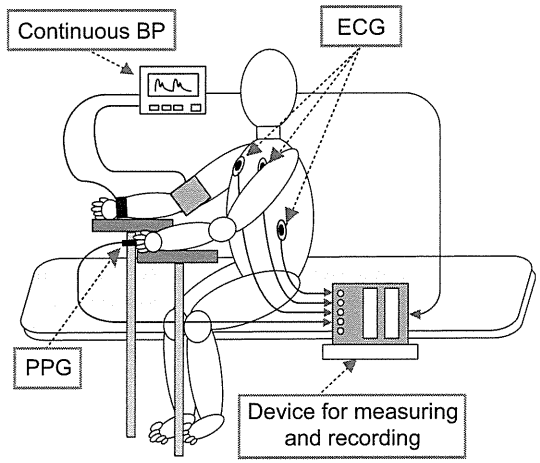

Fig. 3. Setup of experiment with sitting posture

C. Experiment

To evaluate the proposed method, the experiment in which subjects kept the supine posture for 5 minutes and then the sitting posture for 5 minutes under the resting condition, was carried out. The postural change from the supine posture to the sitting posture brings a decrease of blood pressure. Therefore, heart rate is increased by the response of the baroreflex system. We confirmed whether BPV-related information could be obtained from the PPG signal by using the ICA and whether $\rho_{\max}$ calculated from this information could indicate the response caused by the postural change. Healthy 18 subjects (aged 24.2 $\pm$ 3.6) participated in the experiment. Figures 2 and 3 show the setup of the experiment. The subject's ECG, continuous blood pressure, and finger PPG were measured during the experiment.

D. Analyses

On the basis of the observed matrix $\boldsymbol{X}$ obtained from the experiment, the mixing matrix $\boldsymbol{A}$ and the independent component matrix $\boldsymbol{S}$ were calculated with the ICA for each subject. Define n independent component time series IC_l; $l = 1, 2, \ldots, n$ as $IC_l = \{s_l(1), s_l(2), \ldots, s_l(K)\}$ with the data size of K corresponding to the length of the experiment.

Let time series $\rho_{\max}(BP)$ and $\rho_{\max}(IC_l)$ denote $\rho_{\max}$

between HRV and BPV, and $\rho_{\max}$ between HRV and an independent component IC_l, respectively.

Let l_{BP} denote the optimal number of l that minimizes the sum of the root mean square error (RMSE) between $\rho_{\max}(BP)$ and $\rho_{\max}(IC_l)$ and of the RMSE between $\tau_{\max}(BP)$ and $\tau_{\max}(IC_l)$ as follows:

$$l_{BP} = \arg \min_{l=1,\ldots,n} \left[\sqrt{E[\{\rho_{max}(BP) - \rho_{max}(IC_l)\}^2]} + \lambda \cdot \sqrt{E[\{\tau_{max}(BP) - \tau_{max}(IC_l)\}^2]} \right] \quad (7)$$

where λ represents a weighting factor of the term related to $\tau_{\max}$ and is chosen to be 0.1. Because $\rho_{\max}$ changes from 0 to 1, while $\tau_{\max}$ does from 0 to 10. In addition, the number of independent components, n, was empirically set to 4.

III. RESULTS AND DISCUSSION

Seventeen subjects' data out of 18 could successfully be analyzed in the experiment with the supine posture. Figure 4 shows an example of $\rho_{\max}(BP)$ and $\rho_{\max}(IC_{l_{BP}})$ obtained from a certain subject during the supine posture. Each $\rho_{\max}$ is the averaged value every 30s. BPV-related information of this subject could be estimated. An independent component of this subject consists of BPV-related components.

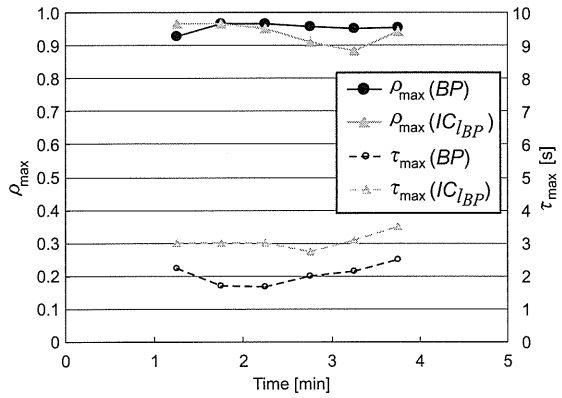

Fig. 4. Example of $\rho_{\max}(BP)$ and $\rho_{\max}(IC_{l_{BP}})$ obtained from certain subject.

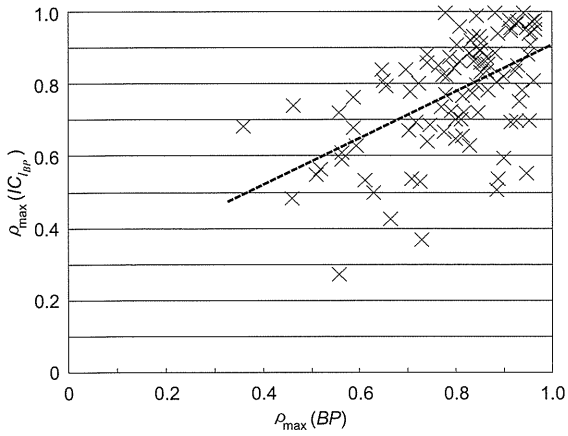

Fig. 5. Comparison between $\rho_{\max}(BP)$ and $\rho_{\max}(IC_{l_{BP}})$ in experiment with supine posture. $r = 0.55$ $(p < 0.01)$

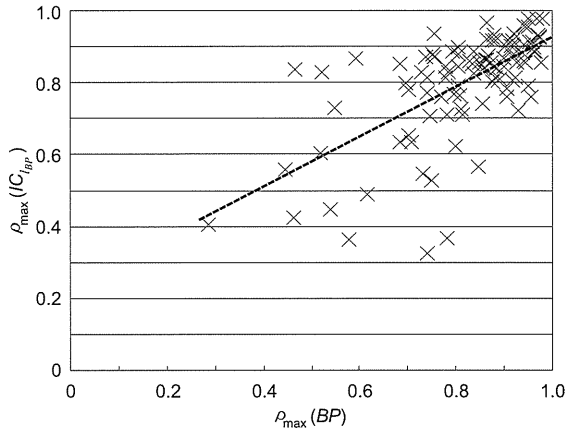

Fig. 6. Comparison between $\rho_{\max}(BP)$ and $\rho_{\max}(IC_{l_{BP}})$ in experiment with sitting posture. $r = 0.65$ $(p < 0.01)$

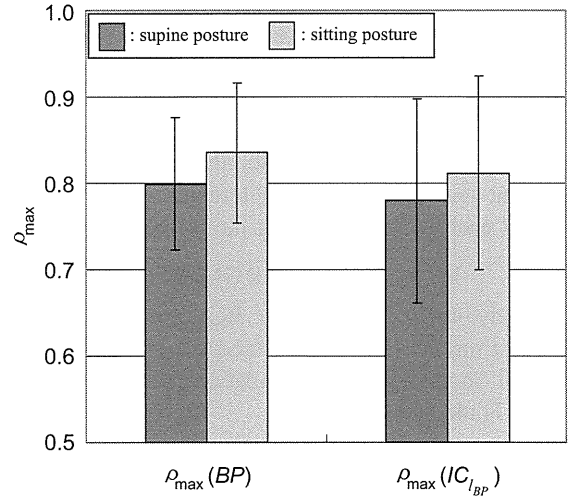

Fig. 7. Comparison between $\rho_{\max}$s of supine posture and of sitting posture.

Figure 5 shows the comparison between $\rho_{\max}(BP)$ and $\rho_{\max}(IC_{l_{BP}})$ during the supine posture. This result indicates that $\rho_{\max}(IC_{l_{BP}})$ correlated significantly with $\rho_{\max}(BP)$ over 17 subjects.

On the other hand, all subjects' data could successfully be analyzed in the experiment with the sitting posture. Figure 6 shows the comparison between $\rho_{\max}(BP)$ and $\rho_{\max}(IC_{l_{BP}})$ during the sitting posture. This result indicates that $\rho_{\max}(IC_{l_{BP}})$ correlated significantly with $\rho_{\max}(BP)$ over 18 subjects.

These results show that the BPV-related parameter could be detected from the PPG feature variables by using the ICA in the experiment of both postures. Thus, it was suggested that the postural change caused little difference in estimation accuracy of BPV.

Figure 7 shows the comparison in $\rho_{\max}$ between the supine posture and the sitting posture. There is no significant difference between $\rho_{\max}$s of two postures. This figure shows that the value of $\rho_{\max}$ of the sitting posture is higher than that of the supine posture. This fact suggests that the postural change caused the response of the baroreflex system, i.e.,

the manipulation of heart rate was activated further by the baroreflex system to regulate blood pressure level against the deviation of blood perfusion caused by gravity.

IV. CONCLUSION

To estimate blood pressure variability, in this study, we have proposed a new method for extracting a blood pressure-related parameter from finger photoplethysmography by using the independent component analysis. From the experimental results, it was ascertained that the proposed method could extract the independent component related to BPV from the PPG signal to yield the maximum cross-correlation coefficient $\rho_{\max}$ between heart rate used for evaluating the state of the autonomic nervous system.

However, we still need blood pressure information to select the index number for the optimal independent component although the mixing matrix will be able to be applied to yield the blood pressure-related parameter based only on the PPG as long as the subject's posture does not change. In the future, we should develop a method for deciding the mixing matrix with photoplethysmography only using other mathematical theory or calculation algorithm for the ICA. In addition, it is important to clarify the characteristics of the baroreflex function of each subject by using the proposed method.

V. ACKNOWLEDGMENTS

This study was subsidized by JKA through its Promotion funds from KEIRIN RACE and was supported by the Mechanical Social Systems Foundation and the Ministry of Economy, Trade and Industry.

REFERENCES

[1] N. Sugita, M. Yoshizawa, M. Abe, A. Tanaka, T. Watanabe, S. Chiba, T. Yambe and S. Nitta, "Evaluation of adaptation to visually induced motion sickness based on the maximum cross-correlation between pulse transmission time and heart rate," *J. Neuroeng. Rehabil.*, vol. 4, p. 35 (online journal; http://www.jneuroengrehab.com/content/4/1/35), 2007.

[2] N. Sugita, M. Yoshizawa, A. Tanaka, K. Abe, S. Chiba, T. Yambe and S. Nitta, "Quantitative evaluation of effects of visually-induced motion sickness based on causal coherence functions between blood pressure and heart rate," *Displays*, vol. 29, pp. 167-175 , 2008.

[3] Abe M, Yoshizawa M, Sugita N, Tanaka A, Chiba S, Yambe T, and Nitta S, "Physiological Evaluation of Effects of Visually-Induced Motion Sickness Using Finger Photoplethysmography," In *Proceeding of SICE-ICASE International Joint Conference*, Busan, Korea, pp. 2340-2343, 2006.

[4] A. Hyvärinen, "Fast and robust fixed-point algorithms for independent component analysis," *IEEE Transactions on Neural Networks*, vol. 10, no. 3, pp. 626-634, 1999.

[5] A. Hyvärinen and E. Oja, "A fast fixed-point algorithm for independent component analysis," *Neural Computation*, vol. 9, pp. 1483-1492, 1997.

生体医工学
47(1)：77-87, 2009

研　究

機械的伸展に対する心筋組織の膜電位応答とその数理モデルによる不整脈シミュレーション

瀬尾　欣也*・稲垣　正司**・平林　智子*・日高　一郎**
杉町　勝**・杉浦　清了*・久田　俊明*

Novel Approach Combining Experiment and Simulation to Clarify the Mechanisms of Stretch-induced Arrhythmias

Kinya SEO,* Masashi INAGAKI,** Satoko HIRABAYASHI,* Ichiro HIDAKA,**
Masaru SUGIMACHI,** Seiryo SUGIURA,* Toshiaki HISADA*

Abstract Mechanical stress is known to alter the electrophysiological property of myocardium and may trigger fatal arrhythmias when an abnormal load is applied to the heart. We developed novel techniques combining experiment and simulation to elucidate the mechanisms of stretch-induced arrhythmias. We applied transient global stretch to arterially perfused rabbit right ventricular wall preparations. The distribution of strain (determined by marker tracking) and membrane potential (measured by optical mapping with the voltage-sensitive dye, di-4-ANEPPS) were simultaneously recorded while accounting for the motion artifact and the 3-D morphology of preparations was examined by the laser scanner. To further investigate the mechanisms of stretch-induced arrhythmogeneicity, we performed a computer simulation based on finite element method (FEM). Although the uniform stretch was applied globally, the medium stretch (10～15%) initiated the excitation from a local spot. On the other hand, the large stretch (> = 20%) caused the synchronous excitation of entire preparation. Computer simulation based on the heterogeneous morphology creates the inhomogeneous strain distribution in response to the stretch, and the focal excitation was observed where the tissue thickness was thin. Our computer simulation also indicates that this focal excitation induced by the medium stretch develop to the stretch-induced spiral wave formation. The inhomogeneous structure of the ventricular wall modulated the globally applied stretch to create heterogeneous strain distribution. Global stretch of medium intensity, rather than intense one, may trigger the fatal arrhythmia.

Keywords: mechano-electric feedback, stretch-activated channels, optical mapping, heart simulation, spiral wave.

1. 序　　論

心臓への機械的伸展がその電気生理学的挙動に影響を及ぼすことは古くから知られており，Mechano-Electric Feedback（MEF）と呼ばれている[1]．心不全や心筋梗塞に見られる心室壁へ異常な負荷のかかる病態において，MEF は正常な心拍リズムを乱す働きをしていると考えられている[2, 3]．このことは，心筋梗塞モデル動物を用いた実験において，梗塞部位と正常部位の境界付近が大きく伸展されることにより不整脈が誘発されるという報告からも支持されるが[4]，機械的伸展のより直接的な関与が示唆されるものに，胸部打撲による突然死，心臓震盪（*commotio cordis*）がある．この突然死の犠牲者の多くは心臓に疾患を持たない若い健常者であり，胸部打撲による肋骨・胸骨・心臓への損傷が見られない[5]．Link らは，麻酔下のブタを使った実験で，野球ボールによる胸部への打撲によって心室細動が誘発されることを明らかにしてお

生体医工学シンポジウム 2008 発表（2008 年 9 月，大阪）
2008 年 7 月 29 日受付，2008 年 10 月 3 日改訂
Received July 29, 2008; revised October 3, 2008.
* 東京大学大学院新領域創成科学研究科
Department of Human and Engineered Environmental Studies, Graduate School of Frontier Sciences, The University of Tokyo
** 国立循環器病センター研究所循環動態機能部
Department of Cardiovascular Dynamics, National Cardiovascular Center Research Institute

り，また，打撲のタイミング・強度・速度が不整脈誘発にどのように影響するかを網羅的に調べている[5].

MEFとそれに起因する不整脈の機序解明のため，これまでにウサギ・ヤギ・イヌなど，さまざまな動物種での実験が試みられてきた[6-8]．一方細胞レベルの研究から，伸展により活性化されるStretch-Activated Channels (SACs) がMEFに深く関与していると考えられており，細胞レベルにおいても機械的刺激によって膜電位がどのように変化するかについて，刺激のタイミング・強度・速度を変えて網羅的に調べられている[9-12]．しかしながら，それら細胞レベルの電気生理学的応答と臓器レベルの不整脈の間の理解には巳然として大きな溝があるのが現状である．

本研究では，伸展に対する膜電位応答という細胞レベルの現象が臓器レベルの不整脈誘発につながるには心室壁の不均質な形状が修飾因子（modulator）として重要な役割を果たしているとの仮説を立て，研究を進めた．この仮説を検討するため，ウサギ右室動脈潅流組織標本に対する光学的膜電位マッピングと，厚み形状を模擬した有限要素法に基づくコンピュータシミュレーションにより検討した．我々はその結果，不均質な組織への伸展刺激によって空間的に不均一な膜電位変化が生じること，特に中程度の伸展刺激に対して不均一性が増強するため致死的不整脈誘発につながる可能性が高いことを示した．

2. 方　　法

2·1 組織標本

日本白ウサギ（n = 7，2.4 kg～2.9 kg）をペントバルビタール（50 mg/kg）麻酔下で開胸し，心臓を素早く摘出した．その後，大動脈をLangendorff潅流装置に接続し，Tyrode溶液（130 mM NaCl，4 mM KCl，1 mM $MgCl_2$，1.2 mM NaH_2PO_4，1.8 mM $CaCl_2$，5.6 mM glucose，and 24 mM $NaHCO_3$）を66mgHgで潅流した．潅流液は95% O_2-5% CO_2でバブリングを行い，37℃，pH = 7.40に調節した．

Tyrode溶液を10分間流して静置させた後，右冠状動脈を切り離さないように注意して弁状に右室自由壁を切り出し，22 mm～20 mm程度の長方形に整えた．組織の両端はシアノアクリレート生体用接着剤（Vetbond™；3M，St.Paul，MN）でサポートに固定した．左端のサポートを単軸伸展装置であるリニアモータ（ET-126A，Labworks Inc.，Costa Mesa，CA，USA）に接続した．このリニアモータには，変位センサー（IW12，TWK-Elektronik，Dusseldorf，Germany）が装着されており，モータの作動距離をパーソナルコンピュータにフィードバックさせて目的の伸展刺激に調節することができる．組織の潅流に対する伸展刺激の影響を極力抑えるため，機械的伸展方向を冠状動脈の走向と一致させた．右端は力センサー（FORT-1000，World Precision Instruments，Sarasota，FL，USA）に取り付け，伸展時の反射張力を測定した．組織を張った状態にするため，反射張力が10gfになる状態を0%伸展（自然長）と定めた．このとき，組織の曲率は非常に小さいため，この条件で組織各所はほぼ均一な状態になっている．ジルコニア製ビーズ（直径0.5 mm）を歪計測用の目印として組織表面に格子状（縦3 × 横4，計12個）に取り付けた．電気刺激による計測部位への直接的影響を避けるため，2本のAg-AgCl電極を左室に取り付けてペーシングを加えた．この際，左室からの電気的興奮は，右室と左室の連結部にある心筋を通して右室自由壁に伝導する．右室自由壁に3本の電極を取り付けて心電図を測定し，その心電図を基に電気刺激時の興奮，機械的伸展時の興奮の有無やタイミングを確認した．測定される信号は12 bitのAD変換機によって2 kHzにデジタル化されパーソナルコンピュータ（PC）のハードディスクに記録した．

全ての実験はGuiding Principles for the Care and Use of Animals in the Field of Physiological Sciences approved by the Physiological Society of Japan and approved by the institutional committeeを遵守して行った．

2·2 光学的膜電位マッピング

装置の模式図を**図1A**に示す．右室動脈潅流組織標本に対する膜電位計測方法は，既に報告されている摘出潅流心での膜電位計測法と同じ手法を用いた[13]．以下簡潔に説明する．組織を膜電位感受性色素di-4-ANNEPS（5μmol/l）を混入したTyrode溶液で20分間潅流する．その後，組織心外膜側を青色発光ダイオード（480 ± 10 nm）で励起し，その反射蛍光をダイクロイックミラーで分離後2つのバンドパスフィルター（540 ± 20 nm，680 ± 20 nm）を通して帯域を絞り，イメージインテンシファイアーを通して信号を増幅させた後CMOSカメラ（FASTCAM-Ultima，Photron，Tokyo，Japan）で測定した．光学画像は500フレーム毎秒，解像度256 × 256で測定し，PCに保存した．実験中，β遮断薬やBDM（2，3-butanedione monoxime）などの心臓の収縮を止める薬剤は使用していない．

2·3 画像処理

伸展や心筋の収縮などの動きによるアーチファクトを測定した光学画像から除去するため，我々は独自に開発したモーション追跡技術とレシオ計算を適用した[13]．簡潔に説明すると，モーション追跡技術については，伸展時の画像と静止時の参照画像において，目印であるビーズとその周辺の画像が一致する場所を相互相関法により探索し，その相対位置を高解像度で決定する．これらの位置情報は2つの目的で使用される．1つは，伸展時のビーズ間の距離を参照配置におけるビーズ間の距離で割ることにより，組織心外膜表面各所の歪を求めることに利用した．2つ目

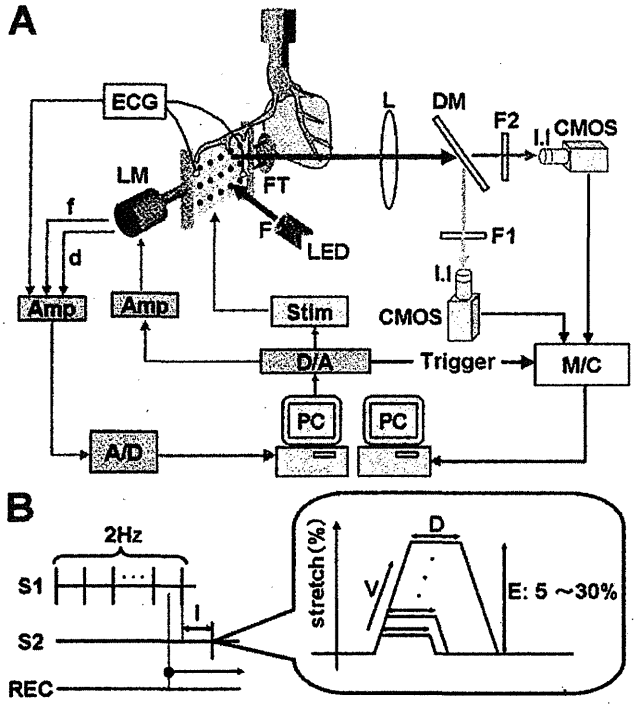

図1 実験装置

A：実験装置の概念図．長方形に整えた右室自由壁の両端を組織サポートに接着固定し，それぞれを力センサー（FT），リニアモータ（LM）に接続した．心電図（ECG），発生張力（f），リニアモータの駆動距離（d）のアナログ信号をアンプで増幅させて（Amp），AD変換機（A/D）を介してパーソナルコンピュータ（PC）に記録した．伸展刺激や電気刺激の出力信号はPCによって生成し，それらはDA変換機（D/A）を通してLMおよび電気刺激装置（Stim）に送られる．光学的膜電位計測では，組織を青色発光ダイオード（LED）で励起し，その反射蛍光をダイクロイックミラー（DM）によって2波長に分離し，2つのバンドパスフィルター（F1，F2）を通して波長帯を絞った．これらの光信号をイメージインテンシファイアー（L1）を通してCMOSカメラ（CMOS）で撮影し，PCのメモリコントローラ（M/C）に保存した．L：lens

B：伸展手順．電気刺激（S1：2 Hz）を与えて組織の状態を安定させ，その後伸展刺激（S2）を加えた．最後のS1とS2の時間間隔を500msec，伸展のプラトー（D）を50msecと一定にした．伸展の大きさ（E）は組織自然長の5，10，15，20，25，30%で与えた．

Fig. 1 Experimental setup.

A：Schematic representation of the experimental setup. Excised RV wall with its intact coronary artery was glued to a pair of tissue supports connected to a force transducer (FT) and a linear motor (LM). ECG, force (f) and displacement (d) signals were amplified (Amp) and recorded by an AD converter (A/D) and personal computer (PC). Stretch and electrical stimulation commands were generated by the PC and applied to LM and electrical stimulator (Stim) through a DA converter (D/A). For optical mapping, the tissue was illuminated by light emission diodes (LED). The fluorescent emission light was split by a dichroic mirror (DM) and narrowed down to the two frequency bands by appropriate filters (F1, F2). The optical images were captured by two independent CMOS cameras (CMOS) with image intensifiers (I.I) and stored in a memory controller (M/C) and PC. L：lens

B：Stretch protocol. A stretch pulse (S2) was preceded by a train of pulses (S1：2 Hz) for stabilizing the tissue condition. The coupling interval between the last S1 and S2 was set to 500 ms, and the duration of stretch (D) was 50 ms. The amplitude of stretch (E) was set at 5, 10, 15, 20, 25 or 30% of the tissue length.

に，この位置情報を基に，伸展あるいは収縮により伴う組織の変形に対してアフィン行列を算出することが可能となる．このアフィン行列を用いることにより，変形時の画像の各点を参照配置に座標変換することができ，膜電位の一連の時間変化を算出し参照配置において表示することが可能になる．また波長540 ± 20 nmの測定データを波長680 ± 20 nmの測定データで割ることにより（レシオ計算），光の経路方向の動きによるアーチファクト（光強度の変化によるアーチファクト）を取り除いた．アーチファクトを除去した光学画像に時空間フィルター処理を行い，最後に興奮の等時線図を作成した．

2·4 伸展方法

伸展刺激を与える手順については図1Bに示した．各測定で，一過性の伸展刺激（S2）を与える前に，組織の状態を安定させるため20回の電気ペーシング（S1：振幅2 mA，刺激時間2 ms）を行っている．伸展刺激のプラトー（D）は50 msに固定し，伸展の大きさは組織全長の5，10，15，20，25，30%としてランダムに与えた．台形の電圧信号をリニアモータに入力し，伸展速度は0.5%で一定にした．最後のS1とS2の間の連結時間（I）は500 msで一定にした．この際，左室へ電気刺激による興奮が右室に伝わるのに時間がかかるが，ECGから500 msの連結時間は，組織が静止膜電位に落ちつくのに十分な時間であることを確認している．

2·5 三次元形状測定

光学的膜電位計測の後，組織標本を左室から切り離し，Tyrode溶液で満たしたチャンバーの底にシアノアクリレート生体用接着剤（Vetbond™；3M，St.Paul，MN）を用いて接着固定した．心筋組織の辺の長さが，膜電位測定時と同じであること，乾燥による厚みの変化がないことを確認した．チャンバーを自動XYステージ（KST-50XY，Sigma Koki，Tokyo，Japan）の上に置き，心内膜表面をレーザー変位測定機（LK-G30，Keyence，Osaka，Japan）でXY方向に0.5 mm間隔で測定し，組織全体の厚み分布をマッピングした．レーザーの屈折による誤差は0.005 mm以下で無視できることを確認している．

2·6 データ分析

組織の興奮確率（y）を伸展率および局所歪（x）の関数として評価する際，次の2つのパラメータを持つロジスティック回帰曲線を用いた：

$$y=\frac{1}{1+\exp(a+bx)}$$

但しa，bは回帰係数とする．

ガドリニウムの効果に関してはA repeated measures ANOVAを用いた．またTukey's testによって有意差を検定した．データは，平均±S.E.Mで表示し，$p<0.05$を統計的に有意であるとした．

2·7　コンピュータシミュレーション

伸展により誘発される不整脈の特徴やその機序をより詳細に検討するため，我々は有限要素法に基づいた独自の組織シミュレーションモデルを作成した[14]．このモデルでは，三次元の構造を63×57×5の要素で構成し，電気・機械現象の数理モデルを各要素に組み込んでいる．モデル形状はレーザー変位計で測定した実験データを基に簡略化して模擬し，不均一な厚み分布を再現した（22×20×2.5～3.5 mm）．この際，各部位の厚みは要素の大きさを変化させることにより調整している．線維方向も組み込み，心内膜側で肉柱に一致させる方向で走行させ（60度），心外膜側にかけて30度ずつ変化させた．心筋の膜電位変化にはLuo-Rudy（LRd）モデルを[15, 16]，組織における興奮伝播にはモノドメインモデルを使用した[17]．MEFの挙動を再現する上では，KohlらのSACモデルを組み込んだ[18]．このモデルではSACsのコンダクタンスが歪の関数になっている．また，このSACモデルでは反転電位が-10 mVになるようにコンダクタンスを設定した．このSACモデルをLRモデルと興奮収縮連関モデルに組み合わせることで，伸展長から細胞内への流入電流量を計算し，膜電位変化をシミュレートすることが可能になる．細胞内カルシウム濃度をクロスブリッジの形成及び収縮力の発生へと結び付けるためには，NegroniとLascanoらの興奮収縮連関モデルを使用した[19]．ここで計算される発生収縮力はLinとYinら超弾性体構成則のパラメータに変換される[20]．構成則は組織全体で均一であるとした．

3.　結　　果

3·1　伸展強度による興奮パターンの変化

伸展刺激により興奮がどのように発生するかを明らかにするために，光学的膜電位マッピング装置を用いて膜電位の空間分布を計測した．図2Aは伸展強度による膜電位変化の典型例である．これらのデータはアフィン変換によって再構築されているため，それぞれの膜電位の経時変化は同一点での連続した変化を表している．小さな一軸方向伸展（5%）を加えた際には，心筋組織は少し脱分極するだけで，活動電位は発生しなかった．（図2A，黒細線）．し

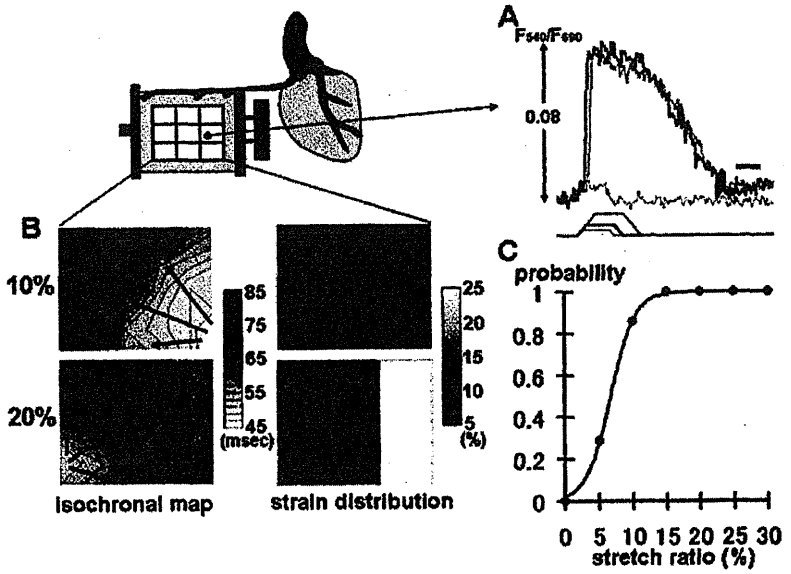

図2　興奮パターンと不均一な歪分布
A：様々な大きさの伸展に対する膜電位応答（F_{540}/F_{680}）．5%（黒細線），10%（黒太線），20%（灰太線）B：左列：興奮伝播の等時線図．右列：局所歪の分布．上段：10%伸展．下段：20%伸展．C：伸展率に対する興奮の誘発率（n = 7）．

Fig. 2　Excitation propagation pattern and inhomogeneous strain distribution.
A：The responses of ratiometric optical signals (F_{540}/F_{680}) in response to uniaxial stretch of various amplitudes (5 (thin black line), 10 (thick black line), 20 (thick gray line) %). B: Left column：Representative isochronal maps of a membrane potential showing the point of initial depolarization. Right column：Distribution of local strain. Upper panel：10% stretch, lower panel：20% stretch. C：The probability that the action potential develops in at least one region of the whole tissue as a function of global stretch (n = 7).

かしながらより大きな伸展では（10～15%），閾値に至るまでは5%伸展と同様膜電位が上昇するが，その後，局所からの興奮誘発が観察された（図2A，黒太線，図2B，上左図）．さらに大きな伸展（>= 20%）では，組織の複数個所あるいは広い領域からの興奮誘発が観察された（図2A，灰太線，図2B，下左図）．図2Cは組織の興奮発生確率（全組織の少なくとも一部で興奮が生じる確率）と伸展率の関係を示したものである．このグラフから伸展率が5～10%の間に急激な興奮確率の変化が確認できる（n = 7）．以上の結果から，興奮はある一定以上の伸展強度で生じるものの，その興奮パターンは異なっていることが示された．

3·2　伸展誘発性期外興奮と局所歪の関係

次に伸展により誘発される興奮の発生箇所と局所歪の関係を評価した（n = 7）．歪分布は組織を9つに分割したそれぞれの領域で平均値を算出し，グレースケールで表示している．異なる強度の伸展刺激を加えた際の歪分布と，それに対応する膜電位の等時線図の一例を図2Bに示す．両者の比較から，興奮は大きな歪箇所から誘発される傾向にあることが示唆された（上段：下右領域14%歪，下段：下左領域14%，上右2領域23%・24%歪）．この傾向はすべての実験における局所歪みと興奮発生確率の関係をまとめた図3Aによっても確認された（n = 7）．さらにこの伸展誘発性の興奮に対するSACsの関与を調べるため，SACsの阻害薬であるガドリニウム投与時の15%伸展刺激に対する応答を調べた．コントロール（CTRL）はガドリニウムが加えられる前の15%伸展に対する応答である．ガドリニウムは伸展誘発性の興奮を71.4%抑制し，またそれをwashoutすることにより興奮は伸展により再び誘発された（図3B，n = 7；$p < 0.01$ vs.control及びwash-out）．

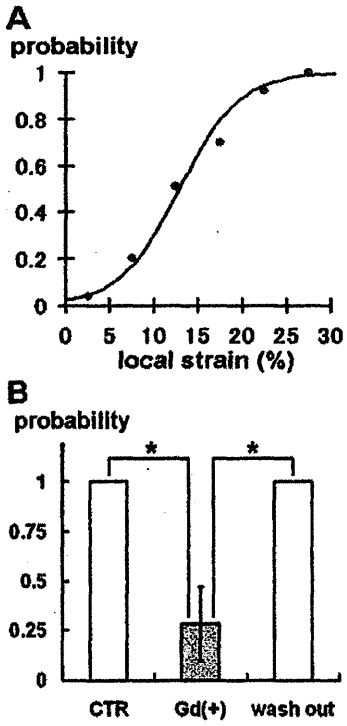

図3　伸展による興奮と薬剤による効果
A：局所における伸展誘発性興奮の発生確率と歪との関係（n = 7）．B：15%伸展おける伸展誘発性興奮に対するガドリニウムの効果（n = 7）．$^*p < 0.01$.

Fig. 3　Excitation by stretch and modulation by the drug.
A：The relation between the probability of stretch-induced excitation in the local area and the strain in the corresponding area (n = 7). B：The effect of Gd^{3+} on the probability of stretch-induced excitation on 15% stretch (n = 7). $^*p < 0.01$.

3·3　不均一な組織形状と歪分布

実験から不均一な興奮パターンが不均一な歪分布に由来することが確認できた．この不均一な歪分布が如何にして生じるのかを確認するため，組織形状を模擬した数理組織モデルを作成した．測定した不均一な三次元厚み形状（図4A）は，図4Bのように簡略化してモデル化した．この作成した組織形状モデルに対して実験と同様の方法で伸展刺激（10%）を加えてそのときの歪分布を計算すると，歪は厚みの薄い箇所で大きくなることが確認できた（図4C）．

3·4　伸展により誘発される致死的不整脈

我々はさらに，これらの不均一な興奮パターンが致死的な不整脈にどのようにして進展するかを調べた．このシミュレーションでは，電気刺激を右端に加えて先行興奮を発生させ，その150～230msec後の各タイミング（5msec間隔で条件を変化させる）で実験と同様に左端から様々な大きさ（5，10，15，20，25，30%）の伸展刺激を加え始め，致死的不整脈誘発の条件を網羅的に調べた（図5）．このプロトコールは正常の心拍に続いて様々なcoupling intervalで急激な伸展が加えられた状況を模擬しており*commotio cordis*の発生する状況を再現している．

その結果，小さな伸展刺激（5%）では，タイミングによらず興奮は誘発されなかったのに対し，中程度の伸展刺激（10%）をあるタイミング（210 msec後）で加えた際には下右部の厚みの薄い局所から興奮が誘発され（250 msec時），それがスパイラル・ウェイブに発展した（図6A）．さらに大きな伸展刺激（20%）では，興奮が広域から誘発され（250 msec），それらはその後410 msecに消失した（図6B）．横軸を伸展長，縦軸を伸展タイミングとして，スパイラル・リエントリ誘発の有無をプロットしたものが図6Cである．これらの結果から，大きな伸展刺激ではなく，むしろ中程度の伸展刺激を再分極相の適切なタイミングで加えた際に，致死的不整脈が誘発されることが示唆された．また，致死的不整脈を誘発する伸展刺激強度は非常に限られた範囲の強度であることが示唆された．

4.　考　　察

本研究では，細胞レベルのMEFが如何にして臓器レベ